Clays and Clay Minerals, Vol. 49, No. 2, 126–140, 2001.

GENESIS OF DIOCTAHEDRAL PHYLLOSILICATES DURING HYDROTHERMAL ALTERATION OF VOLCANIC ROCKS: I. THE GOLDEN CROSS EPITHERMAL ORE DEPOSIT, NEW ZEALAND

DAVID A. TILLICK,[1] DONALD R. PEACOR,[2] AND JEFFREY L. MAUK[1]

[1]Department of Geology, The University of Auckland, Private Bag 92019, Auckland, New Zealand
[2]Department of Geological Sciences, The University of Michigan, Ann Arbor, Michigan 48109-1063, USA

Abstract—To characterize the evolution of dioctahedral interstratified clay minerals in the Golden Cross epithermal deposit, New Zealand, hydrothermally altered volcanic rocks containing the sequence smectite through illite-smectite (I–S) to muscovite were examined by optical microscopy, X-ray diffraction (XRD), scanning electron microscopy (SEM), and transmission and analytical electron microscopies (TEM/AEM).

XRD analyses of 30 oriented clay samples show a broad deposit-wide trend of increasing illite content in I–S with increasing depth and proximity to the central vein system. Six representative samples were selected for SEM/TEM study on the basis of petrographic observations and XRD estimates of I–S interstratification. Ca and Na are the dominant interlayer cations in smectite, but as the proportion of illite layers in I–S increases, so does the K content and (^{IV}Al + ^{VI}Al)/Si ratio. Layers and packets tend to flatten and form larger arrays, reducing the amount of pore space. Smectite coexists with (R = 1) I–S, rather than being (R = 0) I–S where R is the Reichweite parameter. The highest alteration rank samples contain discrete packets of mica to ~300 Å thick, but a limited chemical and structural gap exists between illite, which is intermediate in composition between common illite and muscovite, and illite-rich I–S. Selected-area electron diffraction (SAED) patterns of mica show that the 1*M* polytype dominates, rather than the common $2M_1$ polytype.

Petrographic, SEM, and TEM data imply that all phyllosilicates formed via neoformation directly from fluids. Relatively mature I–S and micas form simultaneously, without progressing through the series of transformations that are commonly assumed to characterize diagenetic sequences during burial metamorphism in mud-dominated basins. Although the overall distribution of clay minerals is consistent with temperature as a controlling variable, local heterogeneities in the distribution of clay minerals were controlled by water/rock ratio, which varied widely owing to different rock types and fracture control.

Key Words—1*M* polytype, Dioctahedral Clay Minerals, Epithermal, Hydrothermal Alteration, Illite-Smectite (I–S), Neoformation, Smectite, Transmission Electron Microscopy (TEM), Volcanic Rocks.

INTRODUCTION

The transition from smectite to illite was inferred by many studies to be a continuous one, *e.g.*, Hower *et al.* (1976) implied that the sequence includes all intermediate I–S structures, with the proportion of illite in interstratified I–S increasing as a function of increasing temperature, time, and burial depth. That view was recently questioned, however, by Dong *et al.* (1997). Based on transmission electron microscope (TEM) data, they inferred that at least for some environments, including the Gulf Coast sequence studied by Hower *et al.* (1976), the sequence is in part discontinuous, with smectite, (Reichweite, R = 1) I–S (50% illite), and illite being the dominant and most stable phases.

Much evidence suggests that the reaction from smectite to illite in diagenetic environments proceeds through a series of Ostwald steps (*e.g.*, reviews of Morse and Casey, 1988; Essene and Peacor, 1995), involving metastable intermediates that result in an end-member mineral assemblage containing muscovite as the dioctahedral phyllosilicate under epizonal (greenschist facies) conditions. The series of steps thus represents a natural progression from metastable phases to an assemblage of thermodynamically stable phases. The theory implies that the number of intermediate states is determined by kinetic factors, as elegantly described by Morse and Casey (1988). Reaction rates may be very different for different rock types; *e.g.*, Niu *et al.* (2000) studied coexisting mudstones and sandstones undergoing burial diagenesis in the Niigata Basin, Japan, and found that reaction progress for smectite illitization proceeded more quickly in the mudstones than the sandstones.

Hydrothermal systems are distinct geologic environments where interstratified clay minerals can form during hydrothermal alteration. Such systems are open to components where convecting fluids produce maximum water/rock ratios, and depths may be shallow (Henley, 1985). More importantly, clays representing the full spectrum of dioctahedral minerals may form at the same time, but at different temperatures. Thus, rather than proceeding through the entire sequence of smectite to I–S to illite and through muscovite, a phase such as illite may crystallize directly from fluids following the dissolution of the original phases such as volcanic glass, as has been proposed for the Salton Sea geothermal system (G. Giorgetti, pers. comm.). Such "episodic" changes in hydrothermal systems may then

have implications for the timing and formation of clay-mineral sequences in basin sediments. It is now recognized, from a large base of geological and geochemical data, that epithermal ore deposits form in the upper <1–2 km of geothermal systems where predominantly meteoric fluids convect and interact with the host rocks at temperatures of ~200–300°C (*e.g.*, Henley and Ellis, 1983; Henley, 1985; Hayba *et al.*, 1985). As consistent with episodic events, geothermal systems are generally relatively short-lived, remaining active over periods of hundreds of thousands of years or less (Henley and Ellis, 1983), though some, such as Steamboat Springs in Nevada, may persist for nearly a million years (Schoen *et al.*, 1974).

X-ray diffraction (XRD) is used extensively to characterize phyllosilicates in hydrothermal systems and to describe interstratification (*e.g.*, Reyes, 1990; Harvey and Browne, 1991; Patrier *et al.*, 1996), stacking order (*e.g.*, Inoue and Utada, 1983), and polytypism (*e.g.*, Inoue *et al.*, 1987). Interstratified dioctahedral phyllosilicates commonly show sequences that reflect hydrothermal zoning. Inoue *et al.* (1978) and Inoue and Utada (1983) studied a complete smectite-to-illite conversion series from the Shinzan hydrothermal alteration area, Japan, in which estimates of percent expandability in I–S, based on XRD data, decreased with depth and increased laterally away from the center of the hydrothermal system. Continuous chemical changes and a systematic increase in the degree of ordering of I–S with decreasing expandability were also reported (Inoue and Utada, 1983).

XRD and TEM are complementary methods in that XRD gives data averaged over relatively large volumes of separated clay fractions, whereas TEM can give local, high-resolution images of specific *in situ* textural relations. Implications for a continuous interstratified sequence from smectite to illite come largely from XRD data, but those for discontinuities are derived from TEM data. Sequences of I–S derived through hydrothermal alteration of volcanic rocks have not been studied by TEM, and therefore textural relations have not been defined. Thus, the nature of clay-mineral transitions is uncertain. Therefore, we have studied here a classic epithermal ore deposit that contains a complete dioctahedral clay-mineral series from smectite through I–S to muscovite, similar to that found in much larger sedimentary sequences such as Texas Gulf Coast shales. Complimentary to this work is a study of the Broadlands-Ohaaki geothermal system (Yan *et al.*, 2001), an active analogue of the Golden Cross ore deposit, in which hydrothermal clay minerals, including smectite, I–S, and illite, are actively forming under hydrothermal conditions. The purpose of the present study is to determine the characteristics of interstratification of I–S using a variety of experimental methods, including petrography, XRD, scanning electron microscopy (SEM), and TEM/AEM (analytical electron microscopy), and the textural relationships among the dioctahedral clay minerals, to characterize the mechanism(s) of formation. Results of various methods, including TEM and XRD, are integrated, and the results compared with clay-mineral sequences in pelitic sedimentary sequences from diagenetic and low-grade metamorphic environments.

GEOLOGIC SETTING AND SAMPLES

Golden Cross epithermal Au-Ag deposit

The Golden Cross low-sulfidation epithermal Au-Ag deposit is located ~8 km northwest of Waihi, New Zealand, in the southern part of the Coromandel Peninsula (Figure 1a). The Coromandel Peninsula consists of Jurassic greywacke basement, overlain by Miocene to early Quaternary calc-alkaline volcanic and volcaniclastic rocks produced by continental arc-type volcanism along a convergent plate margin (Skinner, 1986; Adams *et al.*, 1994). Andesite and subordinate dacite constitute much of the volcanic sequence, with minor rhyolite and ignimbrite occurring along the eastern side of the peninsula (Skinner, 1986). The regional structure is dominated by north-northwesterly and northeasterly trending normal faults, which have block-faulted the graywacke basement (Brathwaite *et al.*, 1989). The peninsula contains mines from the last century of over 50 epithermal Au-Ag deposits.

The Golden Cross deposit is hosted by Coromandel Group andesitic and dacitic lava flows, minor lithic-crystal tuffs, and tuff breccias (Brathwaite and Christie, 1996). Except for a shallow post-ore andesite sequence (Whakamoehau Andesite), the rocks within the deposit have experienced varying degrees of hydrothermal alteration and contain secondary mineral assemblages that include quartz (ubiquitous), adularia (K-rich feldspar), calcite, clay minerals (chlorite, illite or muscovite, kaolinite, interstratified I–S, smectite), pyrite, and minor siderite, apatite, and titanite (de Ronde and Blattner, 1988; Simpson *et al.*, 1998). Hydrothermal alteration, and gold-silver mineralization occurring in fault-controlled banded quartz-veins, is inferred to have occurred between 7.2–6.7 Ma, based on stratigraphic relations (Brathwaite *et al.*, 1989; Brathwaite and Christie, 1996).

Samples

The samples studied consist of 156 hydrothermally-altered volcanic rocks taken from drillcores along three parallel cross-sections through the deposit (4650, 4850, and 5050 m N) and a recently excavated drainage-drive that is beyond the extent of mining. Figure 1b shows the location of the cross-sections relative to the open-pit and the Empire vein. Locations of the samples studied by XRD, SEM, and TEM are shown in Figure 2. Samples are variably altered andesite and dacite lavas and minor tuff breccias, most of which

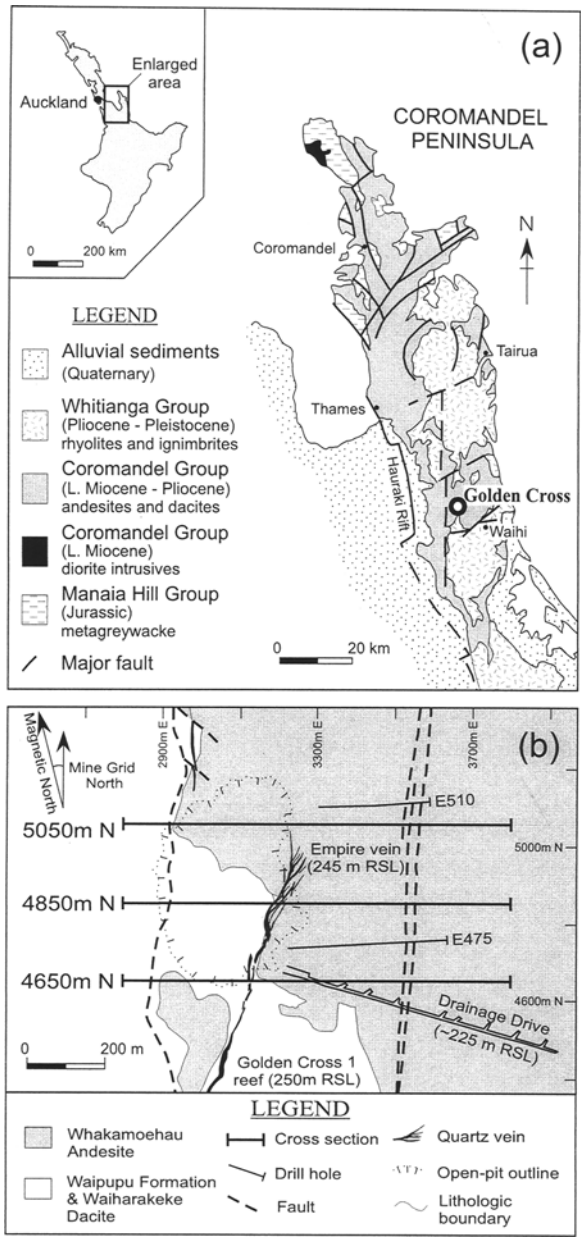

Figure 1. (a) Map showing the location of the Golden Cross deposit, Waihi District, New Zealand (after Skinner, 1986). Inset shows the position of this area in the North Island of New Zealand. (b) Plan view map of the Golden Cross mine area showing the relationship between the open-pit, cross-sections, and Empire vein (modified from Simpson *et al.*, 1998).

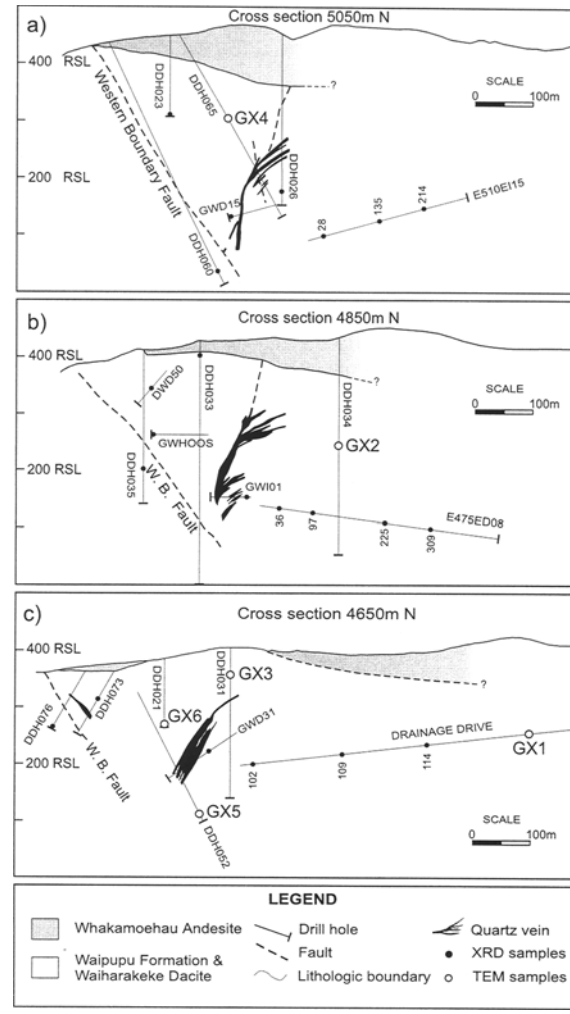

Figure 2. Sample locations along the (a) 5050-m N, (b) 4850-m N, and (c) 4650-m N cross-sections (modified from Simpson *et al.*, 1998).

are intensely and pervasively altered (95–99% secondary minerals; Simpson *et al.*, 1995, 1998) with an estimated 20–40% clay minerals, although rare tuffs may contain >90% clays. The least altered samples generally occur on the periphery of the system and are moderately altered (estimated 10–20% clays). The samples were previously characterized by petrography and XRD analyses in studies that focused on the hydrothermal alteration mineralogy of the deposit (de Ronde and Blattner, 1988; Simpson *et al.*, 1995, 1998). These studies showed that fluid temperatures ranged from ~140°C to >220°C, based on fluid inclusion studies (~220°C dominated), and there is a broad clay-mineral zonation, with illite occurring at depth and surrounding the Empire Vein system, and interstratified I–S (± smectite) occurring in a carapace above, and on the flanks of, the system.

In this study, the samples were thoroughly examined by thin-section petrography to obtain an overview of the mineralogy (*i.e.*, dioctahedral *vs.* trioctahedral), occurrences, and abundance of the clays, based primarily on color and morphology. For XRD analysis, 30 samples were chosen to be representative of the clay minerals and rock types, and to provide lateral and vertical coverage of the varying degrees of alter-

https://doi.org/10.1346/CCMN.2001.0490203 Published online by Cambridge University Press

Table 1. Sample names and XRD estimates of I-S interstratification.

Section	AU#[1]	Drillhole	Depth along hole (m)	XRD			TEM sample
				Clay minerals[2]	I-S °Δ2θ[3]	Percent illite[4]	
4650	46537	DDH021	119.8	Sm, I, Chl/K	—	100	GX6
	46540	DDH031	49.2	I-S, Chl/K, Co	7.16	<70	GX3
	46551	DDH052	322.0	I, Chl/K	8.51	>90	GX5
	46553	DDH073	72.0	Sm, Chl/K	—	—	—
	46560	DDH076	122.0	Chl/K	—	—	—
	46571	GWD31	58.6	I-S, Chl/K	7.60	<80	—
	48601	DR. DRIVE[5]	102.0	I-S, Chl/K	7.06	60	—
	48607	DR. DRIVE	109.0	Sm, Chl/K	—	—	—
	48612	DR. DRIVE	114.0	I-S, Chl/K	7.16	<70	—
	48615	DR. DRIVE	123.0	Sm, Chl/K	—	—	GX1
4850	46581	DDH033	23.3	—	—	—	—
	46587	DDH034	195.9	I-S, Chl/K	5.96	30	GX2
	46590	DDH035	211.6	I, Chl/K	—	100	—
	46605	DWD50a	48.2	Sm, I-S, Chl/K	8.00	<90	—
	46605	DWD50b	48.2	I-S, Chl/K	8.02	<90	—
	46609	GWHOOS	80.1	I, Chl/K	—	100	—
	46611	GWI01	6.3	I-S, K	8.04	<90	—
	48579	E475ED08	36.0	I-S, Chl/K	7.96	<90	—
	48582	E475ED08	97.0	I-S, Chl/K	—	<90	—
	48590	E475ED08	225.0	I, Chl/K	—	100	—
	48597	E475ED08	309.0	Chl/K	—	—	—
5050	46616	DDH023	140.4	I-S, Chl/K	7.92	<90	—
	46621	DDH026	280.2	I, K	8.46	>90	—
	46635	DDH060	368.0	I, Chl/K	—	100	—
	46639	DDH065	158.0	I-S	8.33	90	GX4
	46649	GWD15	87.6	I-S, Chl/K	7.90	80	—
	48564	E510EI15	28.0	I, Chl/K	—	100	—
	48570	E510EI15	135.0	I-S, Chl/K	—	90	—
	48574	E510EI15	214.0	I-S, Chl/K	8.24	<90	—
	48631	D435	269.0	I-S, Chl/K	8.32	90	—

[1] AU#: Auckland University sample number.
[2] Chl: chlorite; Co: corrensite; I: illite; I-S: illite-smectite; K: kaolinite; Sm: smectite.
[3] I-S peak separation: °Δ2θ = °2θ difference between the 001 and 002 peaks of I-S.
[4] Estimates of I-S interstratification using experimental °Δ2θ values and the data of Moore and Reynolds (1997).
[5] DR. DRIVE: Drainage Drive.

ation. A maximum depth of ~430 m below the present land surface was sampled. However, the sample corresponding to this depth (AU46635; Table 1) has experienced an unknown, but likely significant, amount of displacement along the Western Boundary Fault (Figure 2a). The next deepest sample (GX5), from 285 m below the present land surface and ~340–375 m below the inferred paleo-water table (M.P. Simpson, pers. comm.), was not affected by this fault and was therefore chosen as the deepest reliable sample for observations (Figure 2c).

Six samples, GX1 through GX6 (Table 1), were chosen for TEM study to span the range of interstratified I–S compositions as determined by XRD and are numerically ordered, as such, to represent increasing proportions of illite in I–S.

METHODS

XRD data were obtained for oriented clay separates using a Philips PW 1050/25 diffractometer with CuKα radiation (40 kV and 20 mA) and a graphite monochromator. Separates were prepared by gently crushing 1–2 g of rock and dispersing the powder in distilled water containing a diluted deflocculant. Following timed centrifugation, the ≤2-μm fraction of the suspension was transferred with a pipette onto glass slides. Separates were analyzed after air-drying, ethylene glycolation by vapor diffusion, and heating to a maximum temperature of 590°C for 1 h. Proportions of illite and smectite layers in I–S were determined by measuring the separation between the 002 and 003 reflections (Moore and Reynolds, 1997) and were consistent with estimates based on models of several diffraction patterns using the computer program NEWMOD (Reynolds, 1985).

TEM samples were treated with L.R. White resin, following the technique described by Kim *et al.* (1995), to prevent collapse of the expandable layers in the high vacuum of the TEM. Expandable smectite-like layers consequently retain layer spacings of 12–13 Å, allowing them to be distinguished from non-expandable illite-like layers with spacings of 10 Å.

https://doi.org/10.1346/CCMN.2001.0490203 Published online by Cambridge University Press

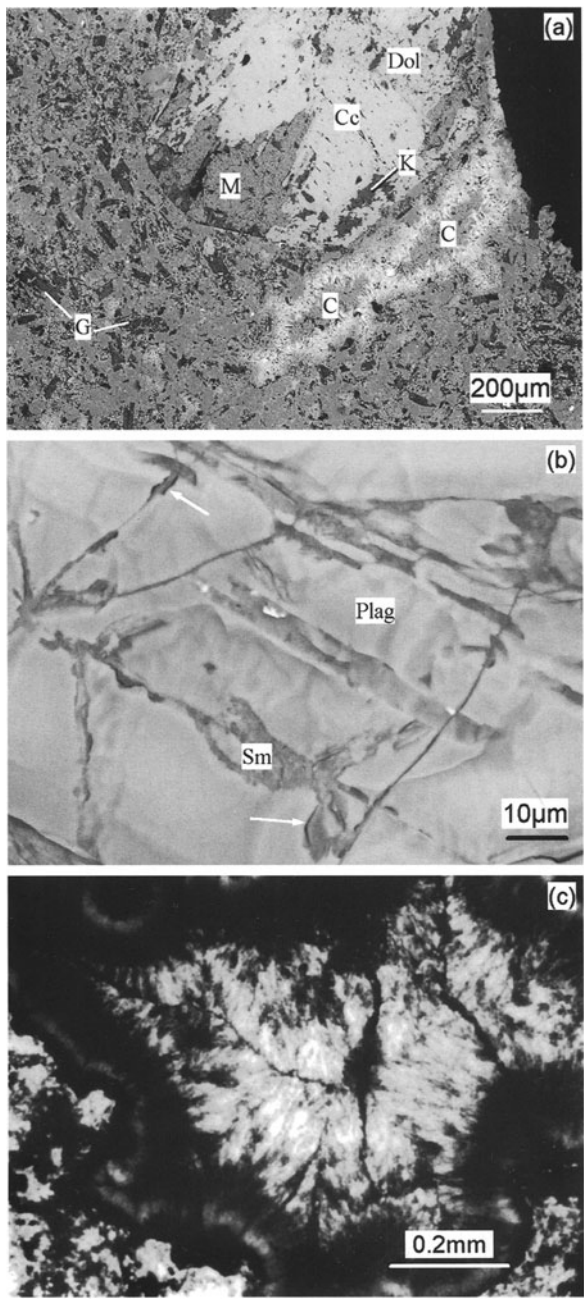

Figure 3. (a) SEM-BSE image of an altered dacite lava sample (GX6) showing the three types of occurrence of clay minerals observed in the samples: 1) The large feldspar phenocryst at the top center has been replaced (*i.e.*, now a pseudomorph) by mica (M), and calcite (Cc), dolomite (Dol), and kaolinite (K); 2) chlorite (bright) and mica (dull) fill cavities (C); and 3) fine clays including smectite and kaolinite occur in the silicified groundmass (G). (b) SEM-BSE image of a partially altered plagioclase feldspar phenocryst in sample GX1 with smectite replacement occurring along microfractures (arrows). Sm: smectite; Plag: plagioclase feldspar. (c) Photomicrograph of cavity-filling chlorite in sample AU46560 (Table 1), illustrating a fabric perpendicular to the cavity walls.

Petrographic and SEM observations were used to select representative areas of thin sections of the treated samples, to which 3-mm diameter aluminum washers were attached. Washer-mounted samples were subsequently removed from the sections and thinned with an argon ion mill. Following carbon coating, backscattered electron (BSE) images and energy dispersive spectral (EDS) analyses of the washer-mounted samples and additional petrographic thin sections were obtained with a Hitachi S-3200N SEM operated at 20 kV. Through-focus TEM observations, from 1000 Å underfocus to 1000 Å overfocus, and AEM analyses of the washer-mounted samples were made mostly at 100,000× magnification on a Philips CM 12 transmission electron microscope equipped with a Kevex Quantum solid-state detector and scanning system. A window size of 200 × 200 nm was used for AEM analyses, and an operating beam current of 10 μA and an accelerating voltage of 120 kV was used for all TEM work.

EXPERIMENTAL RESULTS

Petrographic and SEM observations

Clay minerals display a highly heterogeneous texture at the hand-specimen and microscopic scales. Petrographic and SEM-BSE observations of the clay minerals show that there are three main types of occurrence (Tillick *et al.*, 1999): 1) replacements of mafic and felsic phenocrysts, 2) open-space filling in veins and cavities, and 3) material occurring in the groundmass ('groundmass' being originally comprised of fine-grained igneous minerals and volcanic glass surrounding phenocrysts). Figure 3a illustrates the typical relations between these in a single specimen (GX6). Abundances of these occurrences vary from sample to sample and a given occurrence (generally open-space filling) may be absent from a given sample. Nevertheless, all are present in most samples. Primary volcanic rock textures and structural features such as fractures appear to strongly influence the spatial distribution of the clays in a given sample (Tillick *et al.*, 1999). Despite the common occurrence of these three types of occurrence, no paragenetic sequence could be established. We are not absolutely certain that these three occurrences formed simultaneously, although there is no textural or chemical evidence indicating otherwise. On this basis, the three occurrences probably formed contemporaneously or at nearly identical times. The principal cause for differences in the textures of the clays is decreasing porosity (and therefore water/rock ratio), in the order: open-space filling, granular matrix, and phenocrysts. In such a dynamic system, there were undoubtedly differences in water/rock ratio (among other variables) across the system at a given point in time that have a strong local influence on alteration and clay formation.

https://doi.org/10.1346/CCMN.2001.0490203 Published online by Cambridge University Press

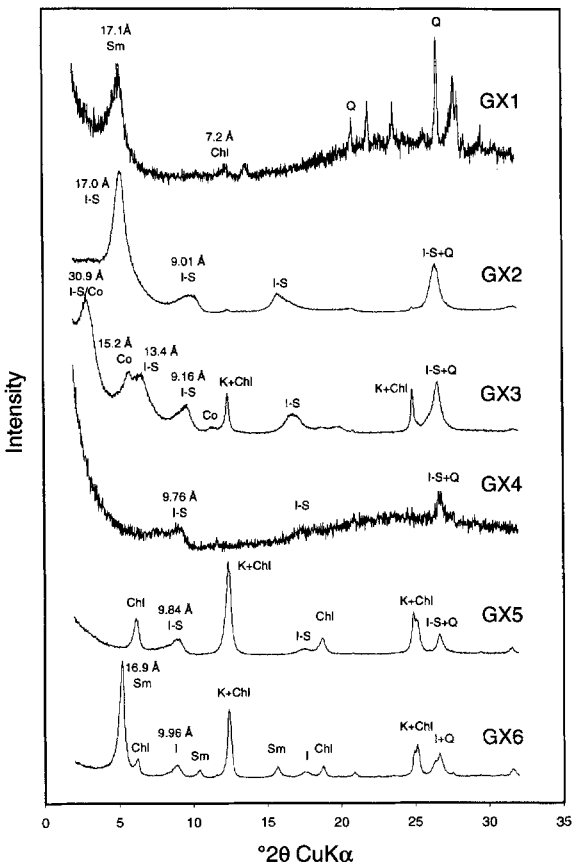

Figure 4. Plot of XRD patterns of ethylene-glycolated ≤2-μm fractions of samples GX1 to GX6, showing clay-mineral peak positions between 2–32°2θ. Vertical scales for each pattern were adjusted to fit. Patterns of samples GX1 and GX4 have lower peak intensities relative to the background than the other samples because suspensions of the clay fraction were more dilute. Chl: chlorite; Co: corrensite; I: illite; K: kaolinite; I–S: illite-smectite; Sm: smectite; Q: quartz.

Phenocryst-replacement material (Figure 3a) is commonly relatively coarse (~5–15 μm clusters in SEM-BSE images) and confined to regions defined by the original outlines of the precursor primary minerals (*e.g.,* plagioclase feldspar, pyroxene, and oxides). Fibrous, optically continuous masses of green to brown chloritic material have directly replaced primary ferromagnesian phenocrysts, whereas some chloritic material with a rosette-like habit presumably crystallized in open cavities formed by dissolution of the phenocrysts. Illitic material replacing phenocrysts displays elongate flame-like or equant platy textures and commonly coexists with secondary calcite, kaolinite, adularia, or quartz. Unlike chlorite, the textural distinction between illitic material directly replacing phenocrysts and illitic material in dissolution cavities is unclear. Illite may replace adularia which formed at the expense of plagioclase feldspar (Simpson *et al.,* 1998). Smectite directly replaced plagioclase phenocrysts in sample GX1. Figure 3b is an SEM-BSE image of smectite occurring along thin microfractures in plagioclase. EDS analyses of this smectite indicate that Ca^{2+} and Na^{+} are the dominant interlayer cations.

Irregularly shaped cavities and veins contain a range of grain sizes, from fine-grained (<2 μm) to coarse-grained (~30 μm) illitic or chloritic clays, typically with flame-like (Figure 3a) or rosette-like textures (Figure 3c). Textures, in many cases, clearly show growth perpendicular to cavity walls or inward coarsening of grain sizes. Several samples contain zoned cavities with alternating bands of clay and non-clay minerals (generally quartz). Kaolinite commonly consists of many juxtaposed crystals comprising stacked hexagonal plates, indicating formation from fluids in open spaces, including phenocryst dissolution cavities. Distinctive vermicular kaolinite was rarely observed.

SEM-BSE observations of fine clays occurring in the groundmass (<2 μm) show small clusters of plate-like grains that are usually associated with fine-grained oxides, quartz, K-rich feldspar, or calcite. EDS analyses of such materials are invariably contaminated with non-clay minerals, but indicate the widespread presence of trioctahedral and dioctahedral clay minerals. Groundmass material always gave compositions with (^{IV}Al + ^{VI}Al)/Si ratios that were smaller than, or equivalent to, the coarser phenocryst-replacement and cavity-filling clays.

X-ray diffraction analyses

The XRD results of this study verify those obtained previously for the same samples (Simpson *et al.,* 1995, 1998). XRD patterns of glycolated oriented separates show evidence for pure smectite, I–S with a wide range of proportions of illite from I–S having ~30% illite to I–S having >95% illite, and illite (Table 1). Figure 4 shows XRD patterns for the samples studied by TEM. There are few samples that have illite proportions in I–S below 50% and the majority that do mainly contain smectite. Above 50% illite content, there is a more continuous, but not complete, range of I–S interstratifications. Interestingly, XRD patterns of sample GX6 have both smectite and illite peaks, consistent with SEM-BSE observations that showed mica in cavities and replacing phenocrysts, and smectite-like minerals confined solely to the groundmass. This indicates that XRD analyses included both groundmass and replacement/cavity-filling clays for at least some of the samples. However, this effect was not examined quantitatively. Kaolinite and chlorite were also present in many of the samples, but the latter had no significant expandable component as it showed no peak shifts with glycolation.

Only one sample, GX3, displays (R = 1) I–S, with a diffraction peak at ~6.6°2θ (13.4 Å) and a superlattice peak at ~3°2θ (30.9 Å). Figure 5 shows a plot of

https://doi.org/10.1346/CCMN.2001.0490203 Published online by Cambridge University Press

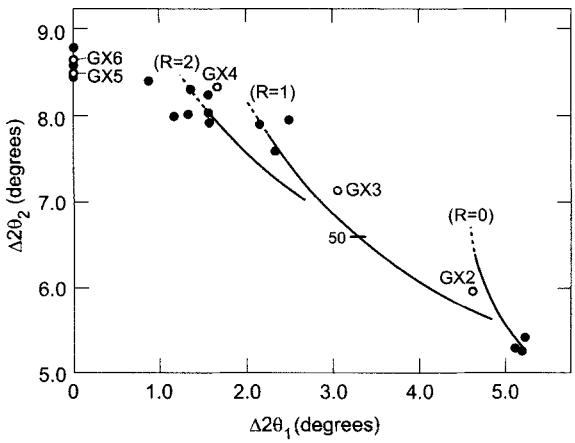

Figure 5. Diagram showing the relationship between $\Delta 2\theta_1$ and $\Delta 2\theta_2$ from XRD patterns of the dioctahedral clay minerals. Curves for R = 0, R = 1, and R = 2 ordering are shown (modified from Inoue and Utada, 1983).

$\Delta 2\theta_1$ and $\Delta 2\theta_2$ for I–S in all samples analyzed for which the appropriate peak positions could be measured. The $\Delta 2\theta_1$ value refers to the difference (in °2θ) between the 001 and 002 peaks of I–S, and the $\Delta 2\theta_2$ value refers to the difference (in °2θ) between the 002 and 003 peaks of I–S. The diagram shows an uneven, discontinuous distribution of I–S interstratification with relatively few samples in the smectite-rich region and near the 50%-expandable region. Many samples plot near the upper extension of the R = 2 curve. Long-range ordering (R > 1), as described by Moore and Reynolds (1997), was apparent for some of the illite-rich samples, where a broad hump was observed on the high-angle side of the 002 peak of I–S at ~8°2θ (11.1 Å; Moore and Reynolds, 1997).

The deposit-wide distribution of interstratified clay minerals shows a general increase in the proportion of illite with increasing depth and proximity to the main vein system (Simpson *et al.*, 1998; Tillick *et al.*, 1999). This increase coincides with an expected thermal gradient caused by rising hot fluids. Several samples do not appear to fit the general trends. For example, sample AU46649 (Table 1) has a lower illite content (~80% illite) than the surrounding samples, although it is much closer (<20 m) to the Empire Vein system where water/rock ratios were high. Likewise, sample GX3 has a lower illite content (~30%) than expected based on its proximity to the vein system. Simpson *et al.* (1998) noted that this sample occurs in a lower-permeability volcanic breccia unit. Thus, variations in permeability (*e.g.*, fracturing) and water/rock ratio probably affect mineral distribution significantly (Tillick *et al.*, 1999).

TEM observations

TEM observations of samples GX1 to GX6 are described in order of increasing illite content.

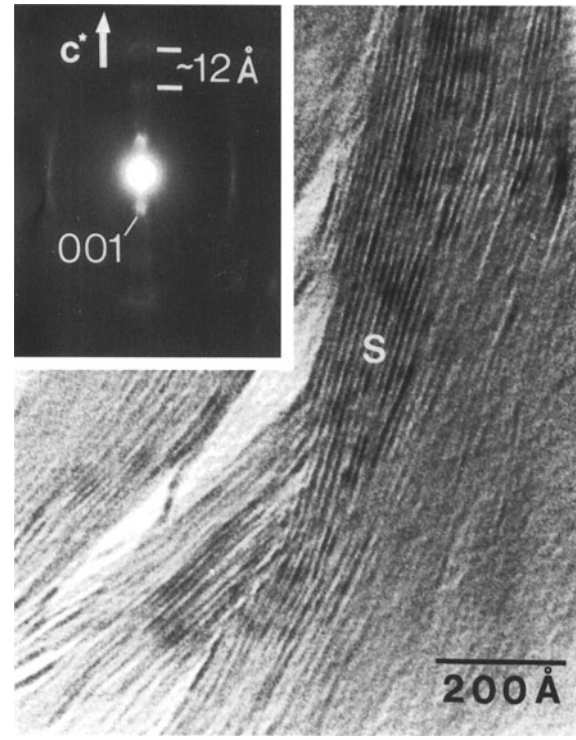

Figure 6. High-magnification TEM lattice-fringe image of smectite in sample GX1, showing typical wavy, anastomosing layers with spacings of 12–13 Å. Inset SAED pattern shows very weak 00*l* diffraction spots that are diffuse in directions normal and parallel to *c**, and extremely diffuse 0*kl* reflections.

GX1: Smectite. Smectite replacing phenocrysts forms packets comprised of typically curved or wavy arrays of parallel to sub-parallel layers, ~50–300 Å thick (Figure 6). Image contrast varies as a result of layer orientation. Fringe spacings are 12–13 Å, which is consistent with the 001 values in XRD patterns of air-dried material, and this implies a lack of change during sample preparation and observation in the TEM. Only weak, diffuse, low-order 00*l* reflections were observed in selected-area electron diffraction (SAED) patterns (inset, Figure 6).

Minor chlorite and/or limited corrensite-like units (24–26 Å) are present that have ill-defined boundaries and are commonly 40–70 Å thick. Such heterogeneity at the TEM scale was commonly observed in replacement and groundmass material. Rare 10-Å layers occur in units to 50 Å thick, but they are more commonly adjacent to smectite-like layers; indicating the presence of local (R = 1) I–S units.

GX2 and GX3: I–S. Figure 7a is a TEM image of I–S in sample GX2, showing an open-space filling within an irregularly shaped cavity. Curved packets or arrays of packets of I–S are shown in sub-parallel orientations that range from ~20 to >500 Å thick. This texture is typical of most material shown by XRD data

https://doi.org/10.1346/CCMN.2001.0490203 Published online by Cambridge University Press

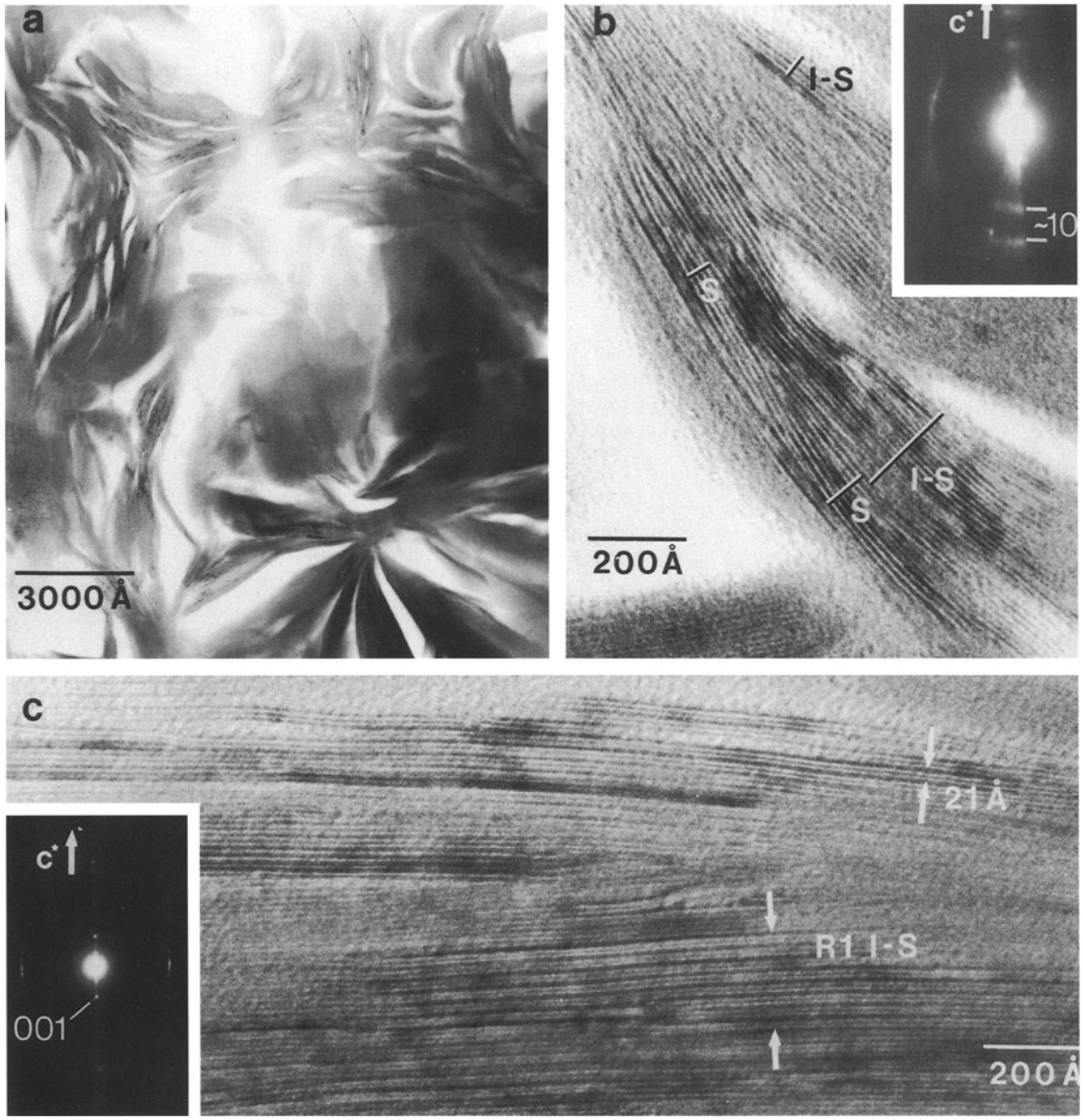

Figure 7. (a) Low-magnification TEM image of sample GX2, showing the typical texture of smectite-rich I–S that has formed in open cavities. Lenticular pores within and between curved packets and arrays of packets are abundant. (b) High-magnification TEM lattice-fringe image of smectite-rich I–S demonstrating the presence of short sequences of one to several IS units. (c) High-magnification TEM fringe image of (R = 1) I–S in sample GX3, showing stacks comprised of several uninterrupted IS units. Inset SAED pattern shows non-periodic 0*kl* reflections with moderate streaking in direction parallel to c^*.

to have <50% smectite layers. As there are for smectite in GX1 (low magnification not shown), there are lenticular pores between and within packets. The I–S is a mixture of dominant (R = 1) I–S and separate smectite, distinguished on the basis of both fringe contrast and fringe spacings, as shown in Figure 7b. Fringe periodicities of smectite and (R = 1) I–S units are typically 12–13 and 21–22 Å, respectively. Some areas show limited sequences of ≤5 uninterrupted (R = 1) I–S units associated with packets of several smectite layers. The inset in Figure 7b is a typical selected area electron diffraction (SAED) pattern in which only low-order, diffuse 00*l* reflections are visible.

Sample GX3 is dominated by (R = 1) I–S and subordinate illite, but lacks discrete smectite. Minor corrensite was observed in TEM images, consistent with the XRD data (Figure 4). Two different textures of

https://doi.org/10.1346/CCMN.2001.0490203 Published online by Cambridge University Press

(R = 1) I–S were observed in low-magnification TEM images. The first is more prevalent in clasts and resembles those in sample GX2, with nearly random orientation of thin packets of (R = 1) I–S and minor illite (≤100-Å thick packets). However, packets are more sharply defined than in sample GX2 and often end abruptly, suggesting that they consist of discrete crystallites of I–S and illite. The second texture is more common in the silicified matrix and consists of larger arrays of (R = 1) I–S (Figure 7c). The arrays are comprised of many sub-parallel to parallel packets of (R = 1) I–S (50% I) with minor interstratification of IIS, IIIS, and other units. SAED patterns of (R = 1) I–S (inset, Figure 7c) show several orders of 00*l* reflections that are only weakly diffuse, but non-periodic diffuse 0*kl* reflections are present, indicating local interlayer coherency.

GX4: Illite-rich I–S. Sample GX4 contains large composite arrays of I–S and illite (≤200 Å thick) consisting of many parallel to sub-parallel packets (Figure 8a). I–S is comprised largely of units with one illite-like and one smectite-like layer (*i.e.,* R = 1), but interstratifications with more illite-like units (*e.g.,* six illite units with a smectite unit) occur randomly. However, short stacks of ≤5 IIS units (31 Å) and ≤3 IIIS (41 Å) units in large arrays of R = 1 were apparent. Little pore space is observed between packets, and packets are generally larger and better aligned than those of more smectite-rich materials.

SAED patterns display several orders of 00*l* reflections that are only weakly diffuse (inset, Figure 8a). Weak 10-Å periodicity of the 0*kl* reflections indicates a high proportion of layers that are coherently or semi-coherently related to 1*M* polytypes.

GX5 and GX6: Mica. Sample GX5 contains composite arrays of illite-rich I–S with larger mica packets, which show sub-parallel to parallel orientations. Packets of mica were common in these arrays (Figure 8b). Mica packets averaged ~130 Å in thickness, but may be to 300 Å.

SAED patterns (inset, Figure 8b) have 0*kl* reflections that display 10-Å periodicity superimposed on weak streaks, indicating coherent domains (*i.e.,* packets of predominantly 1*M* polytypes), but with some stacking disorder. Several packets show two-layer periodicity in images (*e.g.,* $2M_1$ or $2M_2$), but SAED patterns of these areas show numerous low-intensity diffraction spots lacking 20-Å periodicity, even when the sample was tilted to improve orientation.

Figure 8c is a TEM image of mica filling a cavity in sample GX6, illustrating a large array comprised of many parallel or nearly parallel packets with thicknesses of 20–320 Å. Packets consist of straight, relatively defect-free mica layers that display even contrast and layer spacings of 10 Å (Figure 8d). The proportion of natural porosity appears to be small. Sharp, high-order 00*l* reflections are observed in SAED patterns, with no significant streaking or diffuseness, and 0*kl* reflections display 10-Å periodicity that corresponds to 1*M* polytypes (inset, Figure 8d).

AEM analyses

Table 2 shows representative AEM structural formulae of the dioctahedral clay minerals in samples GX1 to GX6. Analyses were obtained from areas that were characterized by lattice-fringe images and electron-diffraction patterns to ensure that material was as homogeneous as possible and free from contaminants. However, owing to the small size of the packets, a small amount of contamination was sometimes inevitable. Data were normalized to 22 oxygen atoms.

AEM analyses show that (^{IV}Al + ^{VI}Al)/Si ratios increase regularly from samples GX1 to GX6, as illustrated in Figure 9. The data plot near a linear trend consistent with an approach towards the composition of muscovite as indicated also by XRD and TEM data. Smectite has an average (^{IV}Al + ^{VI}Al)/Si ratio of 0.37, (R = 1) I-S of 0.64, and mica of 0.87. Analyses of mica in samples GX5 and GX6 are close to ideal end-member muscovite (Figure 9). Such material in both samples GX5 and GX6 has an average net negative charge (nnc) of 1.73 per 22 oxygen atoms.

Figure 10 is a plot of average atoms per formula unit of (a) Al, K, and Si, and (b) Ca, total Fe, Mg, and Na, *vs.* the percentage of illite as determined by XRD. As the percentage of illite increases, K, ^{IV}Al, and ^{VI}Al contents increase and Si content decreases. Smectite contains Ca^{2+} and Na^{+} as dominant interlayer cations (Table 2). Smectite-rich I-S in GX2 contains minimal Na but considerable Ca, suggesting that smectite in smectite-rich I–S also contains interlayer Ca, rather than K. Ca and total Fe generally decrease as the percentage of illite increases, whereas Na and Mg show erratic trends. Sample GX4 has a high Mg value and an anomalously low average total-Al value relative to the other samples, suggesting that I–S may have increased phengitic substitution of Mg^{2+} for Al^{3+} in octahedral sites (the ^{IV}Al/Si ratio is more consistent with the general trends).

DISCUSSION

Summary of observations

The hydrothermally-altered volcanic rocks from the Golden Cross deposit showed that dioctahedral clay minerals of variable crystal size formed *in situ* as open-space filling, replacements of primary phenocrysts, and groundmass replacement. Heterogeneity in the occurrence and distribution of the clay minerals is observed over a range of scales, from the mine face to the TEM scale. XRD data indicate a deposit-wide distribution of interstratified clays broadly consistent with the inferred thermal gradient that prevailed during

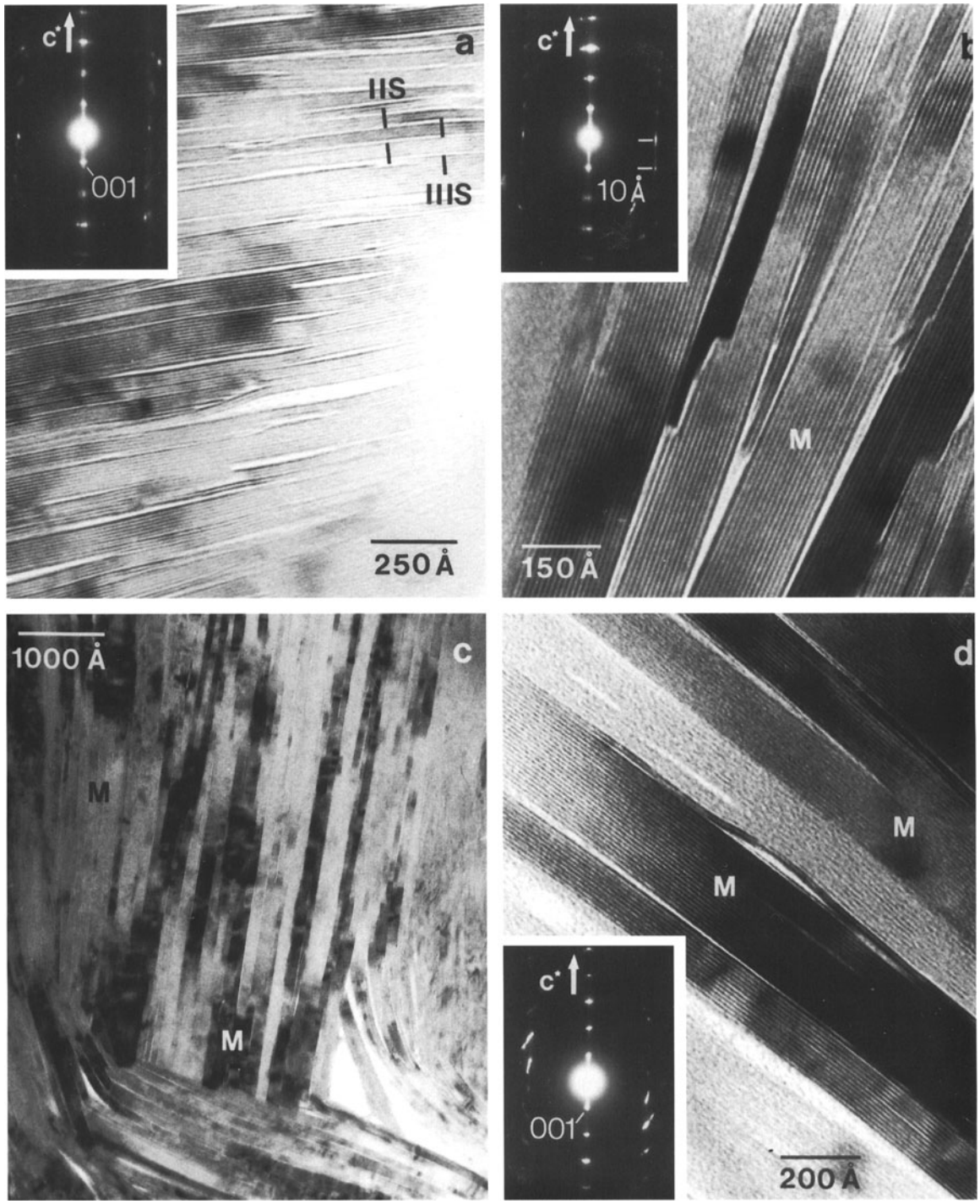

Figure 8. High-magnification TEM lattice-fringe image of illite-rich I–S in sample GX4. Inset SAED pattern shows weak 10-Å periodicity of the 0*kl* reflections. (b) High-magnification TEM lattice-fringe image of mica in GX5. Inset shows SAED pattern of the mica. (c) Low-magnification TEM image of cavity-filling mica in GX6, showing a large array of parallel to sub-parallel packets. The mottled contrast is typical of mica. (d) TEM lattice-fringe image of mica in sample GX6. Inset SAED pattern shows distinct 10-Å periodicity of the 0*kl* reflections. M = mica.

https://doi.org/10.1346/CCMN.2001.0490203 Published online by Cambridge University Press

Table 2. Average AEM structural formulae of smectite, I-S, and illite (muscovite).[1]

	GX1	GX2	GX3	GX4	GX5	GX6
Si	7.48	7.28	6.90	6.81	6.43	6.16
^{IV}Al	0.52	0.72	1.10	1.19	1.57	1.84
^{VI}Al	2.26	3.16	3.33	3.19	3.48	3.53
Fe^{2+}	0.93	0.32	0.30	0.17	0.12	0.16
Mg	0.77	0.44	0.34	0.65	0.40	0.27
Mn	0.03	0.03	0.02	n.d.	n.d.	0.02
Ca	0.29	0.25	0.11	n.d.	0.08	0.02
Na	0.47	0.04	n.d.[2]	0.13	0.25	0.12
K	0.06	0.30	0.85	1.25	1.31	1.55
(^{IV}Al + ^{VI}Al)/Si	0.37	0.53	0.64	0.64	0.79	0.87

[1] Each formula is an average of at least five representative analyses from that sample and is normalized to 22 oxygen atoms. Analyses that showed anomalously high Mg and Fe owing to contamination with chlorite were not included. All Fe is assumed to be ferrous.

[2] n.d.: not detected.

hydrothermal-ore deposition. However, some samples do not fit the deposit-wide trend, suggesting that variables other than temperature are responsible for controlling reaction progress, as discussed in more detail below. SEM and TEM observations of the clay minerals show distinct textural differences with increasing illite content; packets become flatter and more parallel, arrays of packets increase in size, natural pore space decreases, layer contrast becomes more even, and SAED patterns show increasing coherency in layer stacking. These textural changes parallel the AEM data with increasing Al/Si ratios and interlayer K, and decreasing total Fe and interlayer Ca.

Clay mineralogical relations and polytypism

The clay mineralogical relations observed in this study were also observed, with no significant differences, in a parallel study (Yan *et al.*, 2001) of the Broadlands-Ohaaki geothermal system. In brief summary, the combined results include: (1) The observed clay minerals are: (a) smectite, with coexisting (R = 1) I–S. (b) (R = 1) I–S, beginning with near-ideal IS . . . layer sequences, but with increasing proportions of units with larger proportions of illite-like layers, IIS . . . , IIIS . . . , *etc.* (c) illite and mica, with 1*M* polytypes, and nnc intermediate to those of illite typical of sedimentary diagenetic sequences, and muscovite. (2) There is a lack of interstratification of illite-like layers in smectite, and a lack of smectite-like layers in illite-rich material; *i.e.*, there is a nearly complete chemical and structural gap between smectite and (R = 1) I–S, and a more limited gap between (R = 1) I–S and illite. (3) SAED patterns indicate that stacking is largely turbostratic in smectite, with limited coherency in (R = 1) I–S, as indicated by the presence of both *h0l* and 0*kl* streaked reflections in SAED patterns. I–S with high proportions of illite-like layers displays 1*M* polytypism (combined with turbostratic stacking), where-

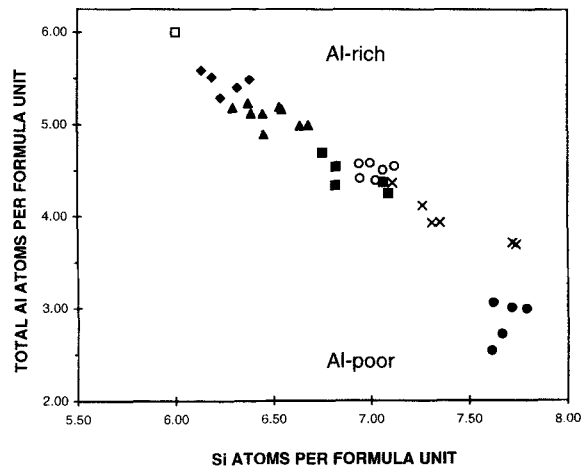

Figure 9. Plot of ^{IV}Al + ^{VI}Al *versus* Si for representative AEM data for samples GX1 to GX6. ●: GX1; ×: GX2; ○: GX3; ■: GX4; ▲: GX5; ♦: GX6; □: position of ideal muscovite.

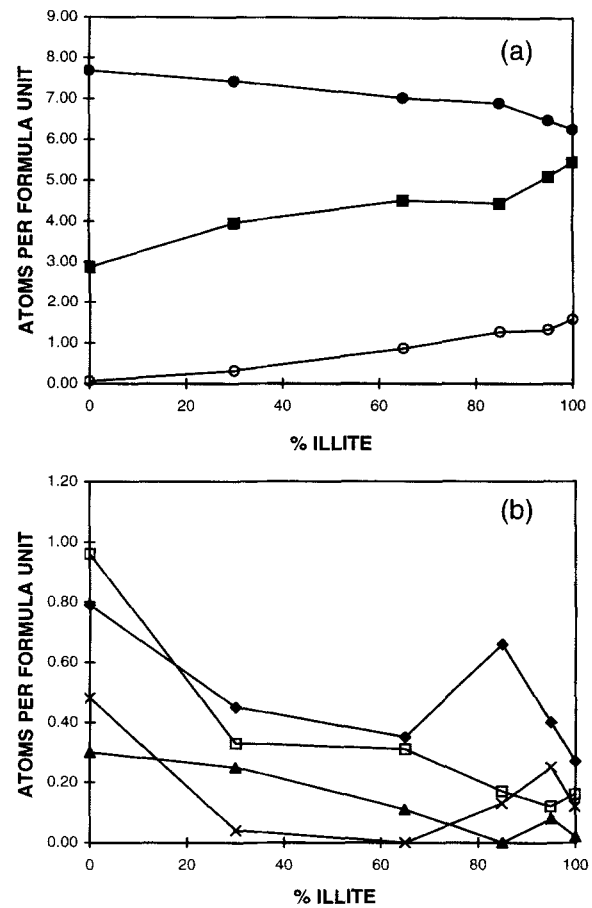

Figure 10. Average AEM structural values of (a) ^{IV}Al + ^{VI}Al, Si and interlayer K, and (b) Ca, total Fe [reported as Fe(II)], Mg, and Na, plotted against the percentage of illite in samples GX1 to GX6 (see Table 2). ■: Al; ♦: Mg; □: Fe; ○: K; ●: Si; ×: Na; ▲: Ca.

https://doi.org/10.1346/CCMN.2001.0490203 Published online by Cambridge University Press

as illite/muscovite packets are largely 1*M*. (4) Interpretations of interstratification based on XRD data are largely confirmed by TEM observations, especially in the approximate proportions of illite-like and smectite-like layers, with the exception of a lack of illite-like layers in smectite, and coexistence of smectite with (R = 1) I-S rather than (R = 0) I–S.

Mechanism of formation

Altaner and Ylagan (1997) reviewed structural models and reaction mechanisms for the smectite-to-illite transition. They described two categories of reaction mechanism; solid-state transformation (SST) and dissolution-crystallization (DC). An SST mechanism involves layer-by-layer replacement of smectite by illite across a reaction front between reactant (smectite) and product (illite), typically via a fluid medium and always accompanied by gradual changes in chemical composition, structure, and texture. The packet-formation mechanism of Ahn and Peacor (1986) is equivalent, except in the simultaneous growth of all packet dimensions, rather than single layers. Hower *et al.* (1976) implied that an SST process occurs in Gulf Coast shale sequences. A DC mechanism, in contrast, proceeds by complete dissolution of the reactant, transport of chemical components in a fluid, and subsequent crystallization of a new phase (I–S) as an epitaxial growth or a separate grain, such that abrupt changes in mineralogy, polytype, and texture are possible. Yau *et al.* (1987) and Altaner and Ylagan (1997), for example, emphasized that SST and DC mechanisms may favor different geologic environments, with SST mechanisms dominating in low-permeability systems, where closed systems are approached (*e.g.,* shales and bentonites), and DC mechanisms in open systems with high water/rock ratios (*e.g.,* hydrothermal systems and sandstones). SST mechanisms are often defined as those where the reactant and product structures are closely related (D. R. Veblen, pers. comm.), as are smectite and illite. As demonstrated by Ahn and Peacor (1986), for example, layer replacement must involve a fluid, albeit at the atomic scale. Thus the SST and DC mechanisms operate via the same process, but at different scales of mineral/fluid interaction.

Collective observations of phyllosilicates at Golden Cross indicate that a neoformation mechanism best describes clay-mineral formation. We emphasize that a general DC mechanism is where mineral components are not necessarily derived by dissolution of preexisting phyllosilicates. More likely, a DC mechanism involves dissolution of primary (or secondary) silicate minerals such as feldspar and pyroxene. The DC mechanism of Altaner and Ylagan (1997) involves essentially the same process but it is applied to a sequence of smectite-to-illite transformations, for which the mineral components forming I–S are probably derived by dissolution of smectite. As we apply the concept, a DC mechanism is not linked to a 'transformation' as normally implied from one clay mineral to another, but to any reactant with a clay mineral as a reaction product.

Our observations indicate that the DC mechanism operated at a variety of scales, even within individual samples. On one hand, petrographic and SEM-BSE images show irregularly shaped cavities and veins, partially or completely filled by clay minerals such as mica (or I–S) and chlorite. Optically, these clays appear as solid radial masses converging towards the centers of cavities or as masses of small equant crystals. Crystal growth in cavities has clearly occurred perpendicular to cavity walls, in a fluid-dominated environment (high fluid/rock ratio) in which the necessary chemical components may have come from beyond the cavity area and were introduced as solutes in a fluid. Similar textures are sometimes apparent in euhedral cavities where clays have crystallized inwards following complete dissolution of the precursor phenocryst. A DC mechanism, probably involving minimal transport of solutes, most appropriately describes these textures and is consistent with the compositional relationship between the precursor mineral (pyroxene or feldspar) and the 'neoformed' clay mineral (chlorite or illite, respectively).

On the other hand, a DC process also appears to have controlled the replacement of phenocrysts by phyllosilicates. SEM-BSE images strongly suggest that the reaction from phenocrysts to phyllosilicates occurred across an extremely small interface between the two. Smectite in sample GX1 (Figure 3b) forms as a replacement product of partially altered plagioclase phenocrysts. Because the structures of the reactant and the product are incompatible, replacement must proceed via a DC mechanism with a fluid at the interface between smectite and plagioclase to facilitate dissolution, transfer/mobilization, and crystallization.

In the partially altered phenocrysts shown in Figure 3b, smectite occurs along permeable microfractures where fluids could reasonably have been able to move and interact with the surrounding crystal. Several studies have proposed K-fixation in smectite prior to I–S formation (Ahn and Peacor, 1986; Inoue *et al.,* 1987; Li *et al.,* 1997). Masuda *et al.* (1996) reported K-rich smectite forming directly as an alteration product of volcanic glass in silicic ash of the Nankai Trough. However, EDS and AEM analyses of the fine smectite in this study indicate that it contains considerable interlayer Na and Ca, but little or no K. Compositions are consistent with the proposed small-scale DC mechanism, whereby Na and Ca cations have been mobilized and incorporated into the forming smectite. Larger areas of smectite in such plagioclase sites generally have exceptionally high Mg and Fe components that reflect TEM observations of thin intergrown packets

of chlorite. Presumably, fluids continued to introduce these elements for chlorite growth as the smectite formed.

The above observations strongly suggest that the same DC mechanism is responsible for both open-space filling and phenocryst replacement, but that the scale differs vastly.

TEM data in support of neoformation

Of hundreds of TEM images examined in this study, none show unambiguous layer-by-layer replacement of smectite-like layers by illite-like layers, regardless of interstratified compositions. Some images are ambiguous in that focus or layer orientation did not allow proper resolution of lattice fringes; these areas were no used to determine layer sequences because of the uncertainty involved in measuring layer spacings. If a layer-by-layer SST mechanism operated, one would expect along-layer transitions to be relatively common in TEM images. Along-layer transitions have been commonly observed by TEM where one phyllosilicate replaced another (Ahn and Peacor, 1987; Jiang *et al.,* 1992) and indeed, provided the most direct evidence for layer-by-layer transformations. We are not aware of any studies that show clear evidence of along-layer transitions from smectite to illite. Ahn and Peacor (1987) noted two-layer units of kaolinite (14 Å) terminating at single biotite layers (10 Å) in partially kaolinitized biotite from schist in Brighton, New Zealand, and showed that it is indeed possible to observe results of fine-scale reactions along layers where they occur.

Although we find no direct evidence for layer-by-layer replacement in the present study, the occurrence of such a process cannot be disproved based only on TEM observations of layer sequences. The relatively common presence of I–S units with R = 2, R = 4, and R = 6 implies that these sequences were not generated by replacement of pure (R = 1) I–S, however, or from short sequences of uninterrupted (R = 1) I–S as observed in sample GX3, as this would result in a mixture of I–S units with R = 1, R = 3, and R = 5. To do so, would involve simultaneous replacement of some smectite layers by illite layers and some illite layers by smectite layers, which is improbable. However, complex sequences of Reichweite ordering such as those in samples GX4 and GX5 (Figure 8a and 8b) could theoretically have formed by replacement of individual smectite-like layers in preexisting mixtures of (R = 1) I–S and smectite (as in sample GX2). Nevertheless, the lack of observation of along-layer transitions is compelling evidence for the lack of such transitions.

Transformation versus simultaneous formation

Many previous studies in diagenetic, low-grade metamorphic, and hydrothermal systems have implied a reaction sequence for the dioctahedral clay minerals involving progressive transformation from smectite to illite over long periods of time. Burial depth, K-availability, temperature, time, and fluid/rock ratio were recognized as the main variables controlling the reaction sequence (*e.g.,* Hower *et al.,* 1976; Whitney, 1990; Christidis, 1995). However, from observations in this study, we propose that clay minerals in hydrothermal systems may form over geologically short periods of time and thus effectively form simultaneously rather than through a series of slow, sequential transformation reactions. Smectite, I–S, and illite are metastable phases and thus are intermediates in a series of reactions that appear to be consistent with the Ostwald step rule (Morse and Casey, 1988; Peacor, 1992; Essene and Peacor, 1995). The degree of local reaction progress via this step rule depends on kinetic factors that control reaction rates (Essene and Peacor, 1995). Thus, I–S, illite, or muscovite could potentially neoform directly from fluids where local kinetic factors such as temperature and fluid/rock ratio provide sufficient 'driving force' to permit activation energies to be partially or completely overcome in the approach to a stable phase, *i.e.,* muscovite. Pathways of smectite illitization in shales, bentonites, and hydrothermal samples were examined by Bethke *et al.* (1986) who showed through junction probability diagrams that the process in hydrothermal samples differed from that in shales and bentonites. Hydrothermal samples showed no mineralogical evidence for a smectite precursor and showed a strong tendency towards maximum ordering, *i.e.,* along a line between rectorite (ordered 50:50 I–S) and illite, not smectite and illite. The data of Bethke *et al.* (1986) imply that (R = 1) I–S (rectorite) may form directly from hydrothermal fluids, rather than through a sequence of transformations beginning with smectite. Their observations are also consistent with the Ostwald step rule and the metastability of smectite, I–S, and illite.

Hydrothermal systems differ from most diagenetic systems insofar as they generally have much higher fluid/rock ratios and greater heat flow concentrated along structural pathways (*e.g.,* faults, fractures). Harvey and Browne (1991) found that fluid-flow type (channel flow and diffuse flow) was the dominant control on the formation of interstratified clay minerals in the active Wairakei geothermal field, New Zealand, noting that a traditional I–S sequence was present in low-permeability lacustrine sediments and breccias, whereas illite and chlorite precipitated directly in fluid-dominated zones. Their observations demonstrate the strong link between fluid/rock ratio and clay-mineral formation in geothermal systems.

Thus, the Golden Cross hydrothermal system represents a distinct geologic environment where clay minerals neoform simultaneously from volcanic materials. Nevertheless, the same overall clay-mineral se-

quence is achieved, and the same stable end-state (muscovite) is approached, as for pelitic sequences in diagenetic low-grade metamorphic environments. As discussed by Yan *et al.* (2001), observation of such a dioctahedral clay-mineral sequence does not therefore provide unequivocal evidence of a continuum of *transformations* of clay minerals from smectite through illite to muscovite. Rather, as in hydrothermal systems such as Salton Sea or Golden Cross, such sequences may have formed during a single event, as was suggested for the "type" sedimentary diagenetic system of the Gulf Coast (Morton, 1985; Ohr *et al.,* 1991).

ACKNOWLEDGMENTS

We thank Coeur Gold New Zealand, Ltd. for access to the Golden Cross deposit and permission to publish this manuscript. This research was supported by the National Science Foundation (NSF; grants EAR-94-18108 and EAR-98-14391) and the New Zealand Foundation for Research, Science and Technology (FRST). D.A. Tillick gratefully acknowledges additional financial support from the Australasian Institute of Mining and Metallurgy (AusIMM) and the Society of Economic Geologists (SEG). We thank C.E. Henderson and L.-S. Kao for technical assistance at the University of Michigan. D.A. Tillick is indebted to B. Bauluz for TEM training, M.P. Simpson for drafting some of the figures, and Y. Yan for her support and ideas. W. Huff and M. Buatier are thanked for helpful reviews of the manuscript. The STEM used in this study was acquired under NSF grant EAR-87-08276 and the SEM under grant BSR-83-14092.

REFERENCES

Adams, C.J., Graham, I.J., Seward, D., and Skinner, D.N.B. (1994) Geochronological and geochemical evolution of the late Cenozoic volcanism of the Coromandel Peninsula, New Zealand. *New Zealand Journal of Geology and Geophysics,* **37,** 359–379.

Ahn, J.H. and Peacor, D.R. (1986) Transmission and analytical electron microscopy of the smectite-illite transition. *Clays and Clay Minerals,* **34,** 165–179.

Ahn, J.H. and Peacor, D.R. (1987) Kaolinitization of biotite: TEM data and implications for an alteration mechanism. *American Mineralogist,* **72,** 353–356.

Altaner, S.P. and Ylagan, R.F. (1997) Comparison of structural models of mixed-layer illite/smectite and reaction mechanisms of smectite illitization. *Clays and Clay Minerals,* **45,** 517–533.

Bethke, C.M., Vergo, N., and Altaner, S.P. (1986) Pathways of smectite illitization. *Clays and Clay Minerals,* **34,** 125–135.

Brathwaite, R.L. and Christie, A.B. (1996) *Geology of the Waihi Area - 1:50,000 Geological Map 21.* Institute of Geological and Nuclear Sciences, New Zealand, 1 sheet and 64 pp.

Brathwaite, R.L., Christie, A.B., and Skinner, D.N.B. (1989) The Hauraki Goldfield-regional setting, mineralisation and recent exploration. In *Mineral Deposits of New Zealand,* D. Kear, ed., New Zealand Geological Survey, Lower Hutt, New Zealand, 45–56.

Christidis, G.E. (1995) Mechanism of illitization of bentonites in the geothermal field of Milos Island Greece: Evidence based on mineralogy, chemistry, particle thickness and morphology. *Clays and Clay Minerals,* **43,** 569–585.

de Ronde, C.E.J. and Blattner, P. (1988) Hydrothermal alteration, stable isotopes, and fluid inclusions of the Golden Cross epithermal gold-silver deposit, Waihi, New Zealand. *Economic Geology,* **83,** 895–917.

Dong, H., Peacor, D.R., and Freed, R.L. (1997) Phase relations among smectite, R1 illite-smectite, and illite. *American Mineralogist,* **82,** 379–391.

Essene, E.J., and Peacor, D.R. (1995) Clay mineral thermometry - A critical perspective. *Clays and Clay Minerals,* **43,** 540–553.

Harvey, C.C. and Browne, P.R.L. (1991) Mixed-layer clay geothermometry in the Wairakei geothermal field, New Zealand. *Clays and Clay Minerals,* **39,** 614–621.

Hayba, D.O., Bethke, P.M., and Foley, N.K. (1985) Geologic, mineralogic, and geochemical characteristics of volcanic-hosted epithermal precious-metal deposits. In *Reviews in Economic Geology, Volume 2: Geology and Geochemistry of Epithermal Systems,* B.R. Berger and P.M. Bethke, eds., Society of Economic Geologists, Chelsea, Michigan, 129–167.

Henley, R.W. (1985) The geothermal framework for epithermal systems. In *Reviews in Economic Geology, Volume 2: Geology and Geochemistry of Epithermal Systems,* B.R. Berger and P.M. Bethke, eds., Society of Economic Geologists, Chelsea, Michigan, 1–24.

Henley, R.W. and Ellis, A.J. (1983) Geothermal systems ancient and modern: A geochemical review. *Earth Science Reviews,* **19,** 1–50.

Hower, J., Eslinger, E.V., Hower, M.E., and Perry, E.A. (1976) Mechanism of burial metamorphism of argillaceous sediments: Mineralogical and chemical evidence. *Geological Society of America Bulletin,* **87,** 725–737.

Inoue, A. and Utada, M. (1983) Further investigations of a conversion series of dioctahedral mica/smectites in the Shinzan hydrothermal alteration area, Northeast Japan. *Clays and Clay Minerals,* **31,** 401–412.

Inoue, A., Minato, H., and Utada, M. (1978) Mineralogical properties and occurrence of illite/montmorillonite mixed layer clay minerals formed from Miocene volcanic glass in Waga-Omono district. *Clay Science,* **5,** 123–136.

Inoue, A., Kohyama, N., Kitagawa, R., and Watanabe, T. (1987) Chemical and morphological evidence for the conversion of smectite to illite. *Clay and Clay Minerals,* **35,** 111–120.

Jiang, W-T., Peacor, D.R., and Slack, J.F. (1992) Microstructures, mixed-layering, and polymorphism of chlorite and retrograde berthierine in the Kidd Creek massive sulfide deposit, Ontario. *Clays and Clay Minerals,* **40,** 501–514.

Kim, J-W., Peacor, D.R., Tessier, D., and Elsass, F. (1995) A technique for maintaining texture and permanent expansion of smectite interlayers for TEM observations. *Clays and Clay Minerals,* **43,** 51–57.

Li, G., Peacor, D.R., and Coombs, D.S. (1997) Transformation of smectite to illite in bentonite and associated sediments from Kaka Point, New Zealand: Contrast in rate and mechanism. *Clays and Clay Minerals,* **45,** 54–67.

Masuda, H., O'Neil, J.R., Jiang, W-T., and Peacor, D.R. (1996) Relation between interlayer composition of authigenic smectite, mineral assembalges, I–S reaction rate and fluid composition in silicic ash of the Nankai Trough. *Clays and Clay Minerals,* **44,** 443–459.

Moore, D.M. and Reynolds, R.C. (1997) *X-ray Diffraction and the Identification and Analysis of Clay Minerals, 2nd edition.* Oxford University Press, New York, 378 pp.

Morse, J.W. and Casey, W.H. (1988) Ostwald processes and mineral paragenesis in sediments. *American Journal of Science,* **288,** 537–560.

Morton, J.P. (1985) Rb-Sr evidence for punctuated illite/smectite diagenesis in the Oligocene Frio Formation, Texas Gulf Coast. *Geological Society of America Bulletin,* **96,** 114–122.

Niu, B., Yoshimura, T., and Hirai, A. (2000) Smectite diagenesis in Neogene marine sandstone and mudstone of the Niigata Basin, Japan. *Clays and Clay Minerals,* **48,** 26–42.

Ohr, M., Halliday, A.N., and Peacor, D.R. (1991) Sr and Nd isotopic evidence for punctuated clay diagenesis, Texas Gulf Coast. *Earth and Planetary Science Letters,* **105,** 110–126.

Patrier, P., Papapanagiotou, P., Beaufort, D., Traineau, H., Bril, H., and Rojas, J. (1996) Role of permeability versus temperature in the distribution of the fine (<0.2 μm) clay fraction in the Chipilapa geothermal system (El Salvador, Central America). *Journal of Volcanology and Geothermal Research,* **72,** 101–120.

Peacor, D.R. (1992) Analytical electron microscopy: X-ray analysis. In *Reviews in Mineralogy, Volume 27, Minerals and Reactions at the Atomic Scale, Transmission Electron Microscopy,* P.R. Buseck, ed., Mineralogical Society of America, Chelsea, Michigan, 113–140.

Reyes, A.G. (1990) Petrology of Philippine geothermal systems and the application of alteration mineralogy to their assessment. *Journal of Volcanology and Geothermal Research,* **43,** 279–309.

Reynolds, R.C., Jr. (1985) NEWMOD - A Computer Program for the Calculation of One-Dimensional Diffraction Profiles of Clays. Published by the author, 8 Brook Road, Hanover, New Hampshire.

Schoen, R., White, D.E., and Hemley, J.J. (1974) Argillization by descending acid at the Steamboat Springs, Nevada. *Clays and Clay Minerals,* **22,** 1–22.

Simpson, M.P., Simmons, S.F., Mauk, J.L., and McOnie, A. (1995) The distribution of hydrothermal alteration minerals at the Golden Cross epithermal Au-Ag deposit, Waihi, New Zealand. In *Pacrim Congress '95,* J.L. Mauk and J.D. St George, eds., Australasian Institute of Mining and Metallurgy, New Zealand, 551–556.

Simpson, M.P., Mauk, J.L., and Simmons, S.F. (1998) The occurrence, distribution and XRD properties of hydrothermal clays at the Golden Cross epithermal Au-Ag deposit, New Zealand. In *Proceedings of the 20th New Zealand Geothermal Workshop, Auckland, New Zealand,* S.F. Simmons, ed., Auckland University Geothermal Institute, New Zealand, 215–220.

Skinner, D.N.B. (1986) Neogene volcanism of the Hauraki Volcanic Region. In *Late Cenozoic Volcanism in New Zealand,* I.E.M. Smith, ed., Royal Society of New Zealand Bulletin 23, New Zealand, 21–47.

Tillick, D.A., Mauk, J.L., and Peacor, D.R. (1999) SEM and TEM investigations of a dioctahedral clay mineral series in the Golden Cross epithermal deposit, New Zealand: Preliminary results. In *Proceedings of the 32nd Annual Conference, New Zealand Branch of the Australasian Institute of Mining and Metallurgy, Bay Of Islands, New Zealand,* Australasian Institute of Mining and Metallurgy, New Zealand, 131–140.

Whitney, G. (1990) Role of water in the smectite-to-illite reaction. *Clays and Clay Minerals,* **38,** 343–350.

Yan, Y., Tillick, D.A., Peacor, D.R., and Simmons, S.F. (2001) Genesis of dioctahedral phyllosilicates during hydrothermal alteration of volcanic rocks: II. The Broadlands-Ohaaki hydrothermal system, New Zealand. *Clays and Clay Minerals,* **49,** 141–155.

Yau, Y-C., Peacor, D.R., and McDowell, S.G. (1987) Smectite-to-illite reactions in Salton Sea shales: A transmission and analytical electron microscopy study. *Journal of Sedimentary Petrology,* **57,** 335–342.

Email of corresponding author: DTillick@anaconda.com.au

(*Received 22 February 2000; accepted 12 August 2000; Ms. 428; A.E. Peter J. Heaney*)